

Article

Surface Engineering of $\text{WO}_3/\text{BiVO}_4$ to Boost Solar Water-Splitting

Yuncheng Cao ^{1,2,†}, Zheng Xing ^{3,†}, Bobo Wang ², Wei Tang ², Rong Wu ^{1,*}, Jiangyu Li ^{2,*} and Ming Ma ^{2,*}

¹ School of Physics Science and Technology, Xinjiang University, Urumqi 830046, China; caoyunchengxju@163.com

² Shenzhen Institutes of Advanced Technology, Chinese Academy of Sciences, Shenzhen 518055, China; bb.wang1@siat.ac.cn (B.W.); wei.tang1@siat.ac.cn (W.T.)

³ Schulich Faculty of Chemistry, Technion-Israel Institute of Technology, Technion City, Haifa 3200008, Israel; xingzheng88@hotmail.com

* Correspondence: wurongxju@sina.com (R.W.); jy.li1@siat.ac.cn (J.L.); ming.ma@siat.ac.cn (M.M.)

† These authors contribute equally.

Received: 28 April 2020; Accepted: 14 May 2020; Published: 18 May 2020



Abstract: Single-phase photoanodes often suffer inferior charge transport, which can be mitigated by constructing efficient heterojunctions. Thus, we have fabricated a fluorine-doped tin oxide (FTO)/ $\text{WO}_3/\text{BiVO}_4$ heterojunction using hydrothermal and spin-coating methods. Surface engineering was exploited to further accelerate the reaction kinetics, which was achieved via post-modification with NaOH solution. This treatment alters the surface chemical state of the BiVO_4 nanoparticles, leading to enhanced charge transport and surface water oxidation processes. As a result, the optimized sample can produce a photocurrent more than two times that of WO_3 . The simple post-treatment provides a viable and cost-effective strategy for promoting the photoelectric properties of photoanodes.

Keywords: FTO/ $\text{WO}_3/\text{BiVO}_4$ heterojunction; photoelectrochemical; post-modification; surface engineering; solar water-splitting

1. Introduction

In recent decades, global energy consumption resources have been dominated by fossil fuels. Fast economic growth is accompanied by high energy demand and environmental pollution. To solve the above issues, the development of renewable energy resources has become a top priority. Hydrogen, as a clean fuel, is a promising alternative to fossil fuels in the near future. Based on the pioneering work by Fujishima and Honda [1], photoelectrochemical (PEC) systems have been constructed using semiconductors to split water and generate hydrogen under solar illumination [2–5]. The solar conversion efficiency depends on the physiochemical properties of semiconductors, such as light absorption range, charge migration mobility, and surface catalytic kinetics. To date, various metal oxides have been discovered for PEC water-splitting purposes, such as ZnO [6], BiVO_4 [7], TiO_2 [8], and WO_3 [9]. However, single-component materials often suffer inferior charge transport and severe charge recombination [10,11]. In this regard, constructing efficient heterojunction structure could be a competent strategy to improve solar water-splitting due to the synergistic effect of two or more materials [12].

WO_3 is well known as a promising photoanode material due to its relatively small band gap (about 2.5–2.8 eV) and thus good visible light response [13,14]. In addition, owing to its non-toxicity, simple fabrication protocols and excellent stability in acidic solution [15], WO_3 has been extensively investigated for PEC water-splitting. However, the shortcomings of WO_3 are still present, such as

severe charge recombination and slow migration rate of the photo-generated charge carriers [16]. Compared with other modification methods, the construction of heterojunctions with WO_3 seems more efficient for both promoting the visible light response and charge separation [17]. For example, Zhang et al. built a $\text{WO}_3/\text{Cu}_2\text{O}$ heterojunction through electrochemical deposition to modify the photoelectric properties of WO_3 and achieved $1.37 \text{ mA}/\text{cm}^2$ at 0.8 V vs. reversible hydrogen electrode (RHE) [18]. However, the instability and toxicity of Cu_2O restrict its practical application. BiVO_4 provides a suitable heterojunction companion for WO_3 , thanks to its relatively narrow band gap and environmental benignness [19–21]. Even though numerous research works have been done on $\text{WO}_3/\text{BiVO}_4$ heterojunctions, the sluggish surface reaction kinetics of BiVO_4 still hinders further industrial application for solar conversion [22,23].

Several methods have been employed to modify the surface chemistry, such as elemental doping, introduction of oxygen vacancies, and deposition of passivation layer. For example, Wang et al. prepared BiVO_4 with rich oxygen vacancies through electrodeposition and heat treatment to enhance the surface reaction kinetics for solar conversion [24]. Ye et al. deposited $\text{NiOOH}/\text{FeOOH}$ and CQDs (carbon quantum dots) on the surface of BiVO_4 through multiple fabrication processes and successfully improved the photo-response range and surface reaction activity of BiVO_4 [25]. However, those reported methods always involve highly complex processes. In this work, we implemented a simple post-modification strategy using sodium hydroxide solution to conduct mild treatment for fluorine-doped tin oxide (FTO)/ $\text{WO}_3/\text{BiVO}_4$ heterojunction, with the fabrication processes shown in Figure 1. Surface burnishing occurred to the treated FTO/ $\text{WO}_3/\text{BiVO}_4$ samples, which increased the conductivity and surface reactivity of FTO/ $\text{WO}_3/\text{BiVO}_4$ heterojunction. Compared to previous reports on $\text{WO}_3/\text{BiVO}_4$ [26–30], our work focused on the surface modification through simple and mild method. The optimized FTO/ $\text{WO}_3/\text{BiVO}_4$ sample showed improved photocurrent density of about $1.75 \text{ mA}/\text{cm}^2$ at 1.23 V vs. RHE.

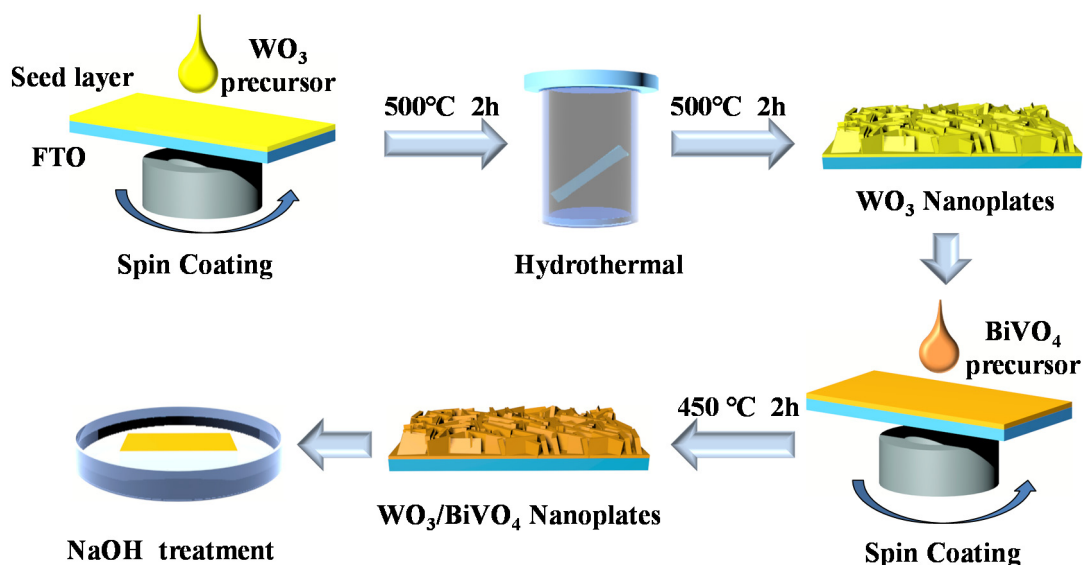


Figure 1. Schematic diagram of the fabrication and post-modification processes of $\text{WO}_3/\text{BiVO}_4$ photoanodes.

2. Results and Discussion

2.1. Morphology and Structure of FTO/ $\text{WO}_3/\text{BiVO}_4$ Heterojunction

To grow WO_3 nanoflakes, FTO glass was pretreated to enhance the surface hydrophilicity and used as a conductive substrate. WO_3 seed films on FTO substrates were first prepared via spin-coating followed by thermal annealing [31]. Subsequently, WO_3 nanoflakes were grown on the WO_3 seed films through the hydrothermal method with further thermal annealing to increase the crystallinity.

The microstructure of WO_3 nanoflakes can be clearly observed from the SEM images in Figure 2a and Figure S1, which demonstrate the relatively uniform thickness of the nanoflakes. BiVO_4 precursor was spin coated on top of the WO_3 nanoflakes to fabricate FTO/ WO_3 / BiVO_4 heterojunctions. The amount of BiVO_4 can be tuned by simply adjusting the number of coating cycles. Three kinds of FTO/ WO_3 / BiVO_4 samples were prepared with 3, 7, and 15 coating cycles, which were referred to as WB-3cycle, WB-7cycle, and WB-15cycle. The SEM images of WB-3cycle, WB-7cycle, and WB-15cycle are shown in Figure 2b–d, respectively. Small BiVO_4 particles were formed on the surface of WO_3 nanoflakes for WB-3cycle and WB-7cycle, but the overloading of BiVO_4 for WB-15cycle caused severe aggregation of BiVO_4 particles, which is not ideal for the heterojunction.

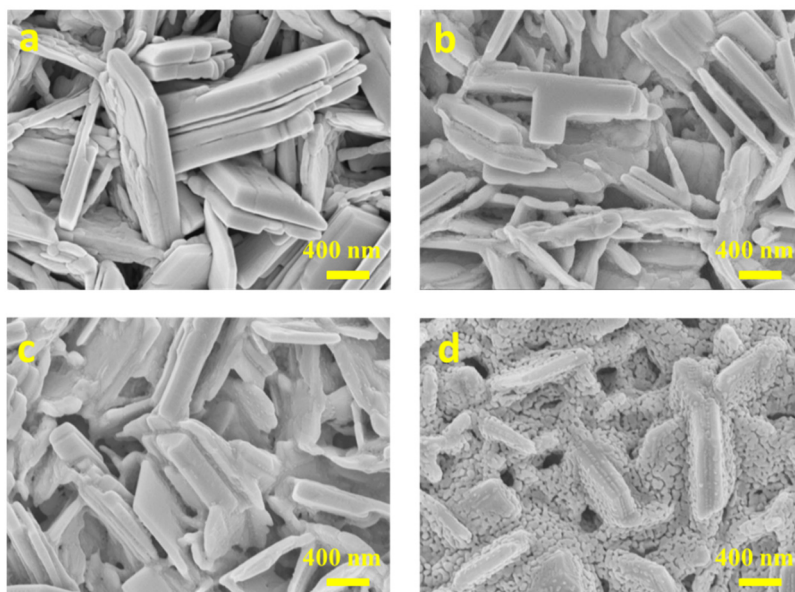


Figure 2. SEM images of (a) WO_3 , (b) WB-3cycle, (c) WB-7cycle and (d) WB-15cycle.

Since WB-7cycle showed the optimum PEC performance, which will be described later, further modifications were only conducted with WB-7cycle. WB-7cycle was immersed in a NaOH solution for different times of 30 s, 5 min and 10 min, and the obtained samples were referred to as WB-30s, WB-5min, and WB-10min, respectively. The SEM images of the treated FTO/ WO_3 / BiVO_4 samples are shown in Figure S2. From the results, almost no difference could be observed for the treated FTO/ WO_3 / BiVO_4 samples when compared to WB-7cycle.

XRD patterns were measured to confirm the phase composition and crystal structure. Figure 3a shows the XRD patterns of FTO substrate, WO_3 nanoflakes, and WB-7cycle with standard XRD peaks of WO_3 and BiVO_4 . Pure BiVO_4 was also measured as a comparison (Figure S3). The WO_3 nanoflakes possessed a monoclinic structure (PDF#43-1035) with good crystallinity. The peaks at 23.1° , 23.6° , 24.4° , 33.3° , 34.2° , 41.9° , 50.0° and 56.0° could be indexed to the (002), (020), (200), (022), (202), (222), (140) and (420) planes, respectively. For WB-7cycle, XRD peaks at 18.9° , 28.9° , 30.5° and 47.3° could be as assigned to the (011), (121), (040) and (042) planes of BiVO_4 (PDF#14-0688), respectively. Figure 3b provided the XRD patterns of WB-3cycle, WB-7cycle, and WB-15cycle containing different amount of BiVO_4 . With the increase of the BiVO_4 particles, the typical XRD peaks at 19.0° , 28.9° of BiVO_4 were intensified, confirming the well loading of BiVO_4 particles on the surface of WO_3 nanoflakes. In addition, the XRD patterns of the treated FTO/ WO_3 / BiVO_4 samples were measured and shown in Figure 3c. After treatment with NaOH solution, the peak intensity of (002) plane for WO_3 decreased. According to previous reports, the (002) facet of WO_3 is more active than other facets for photoconversion [32,33]. Thus, prolonged NaOH treatment may cause deteriorated PEC performance due to the damage of the (002) facet. The optical properties of the FTO/ WO_3 / BiVO_4 structure were

measured with UV-vis absorption spectrophotometer. As shown in Figure 3d, the absorption edge of the WO_3 nanoflakes is around 470 nm. After the introduction of BiVO_4 particles, the absorption range was extended to around 520 nm for WB-7cycle. WB-5min, as the best PEC performer, possessed similar absorption range and intensity with that of WB-7cycle, demonstrating that post-modification did not cause obvious change in absorption. The band gap of WO_3 , WB-7cycle, and WB-15min are estimated to be 2.75, 2.45 and 2.48 eV by Tauc's formula [34] in the Figure S4. In addition, according to previous reports about the band position calculation (details shown in supporting information) [35,36], the charge transfer diagram of the FTO/ WO_3 / BiVO_4 sample was drawn and shown in Figure S5.

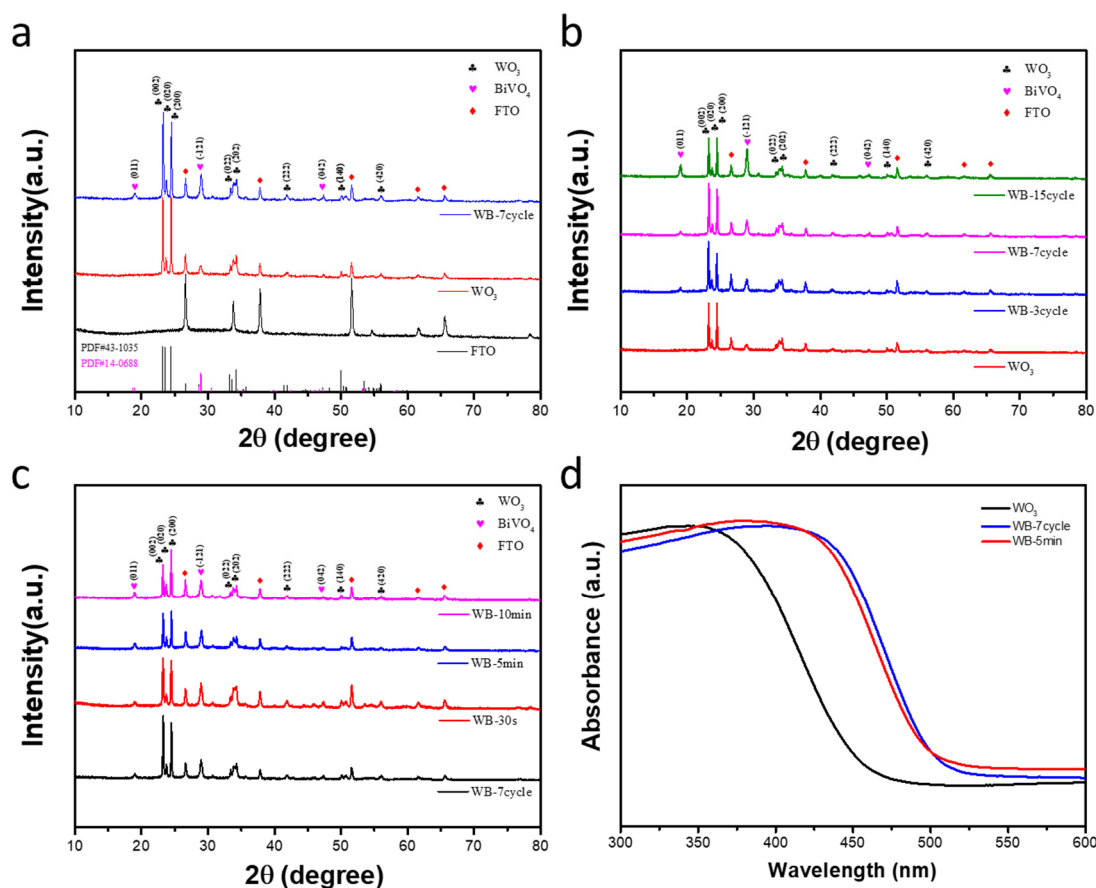


Figure 3. XRD patterns of (a) FTO substrate, WO_3 nanoflakes and WB-7cycle samples with standard XRD peaks of WO_3 and BiVO_4 , (b) WO_3 nanoflakes, WB-3cycle, WB-7cycle, and WB-15cycle and (c) WB-7cycle, WB-30s, WB-5min, and WB-10min samples. (d) UV-vis absorbance spectra of WO_3 nanoflakes, WB-7cycle, and WB-5min.

2.2. Photoelectrochemical Measurement

Photocurrent densities were collected for WB-3cycle, WB-7cycle, WB-15cycle and WO_3 nanoflakes to find the best loading condition of BiVO_4 (Figure 4a). From the I-V (current density-voltage) curves, WO_3 nanoflakes generated a photocurrent density of 0.8 mA/cm^2 at 1.23 V vs. RHE and it can be observed that the current was initially boosted with the increase of BiVO_4 . However, WB-15cycle produced even lower photocurrent than WO_3 did. This should be due to the fact that the excessive BiVO_4 caused severe charge recombination between the BiVO_4 particles [37], inhibiting the charge transfer. Among all samples, WB-7cycle generated the highest photocurrent density of 1.52 mA/cm^2 at 1.23 V vs. RHE. To further enhance the PEC activity of the heterojunction, WB-7cycle was immersed in a NaOH solution for different times. The I-V curves of these samples are shown in Figure 4b. We find that the photocurrent density of WB-5min reached the highest value of 1.76 mA/cm^2 at 1.23 V vs. RHE.

Prolonged treatment, i.e., 10 min, led to declined photocurrent, especially in the low potential range, possibly due to the damage to the (002) facet of WO_3 by NaOH treatment.

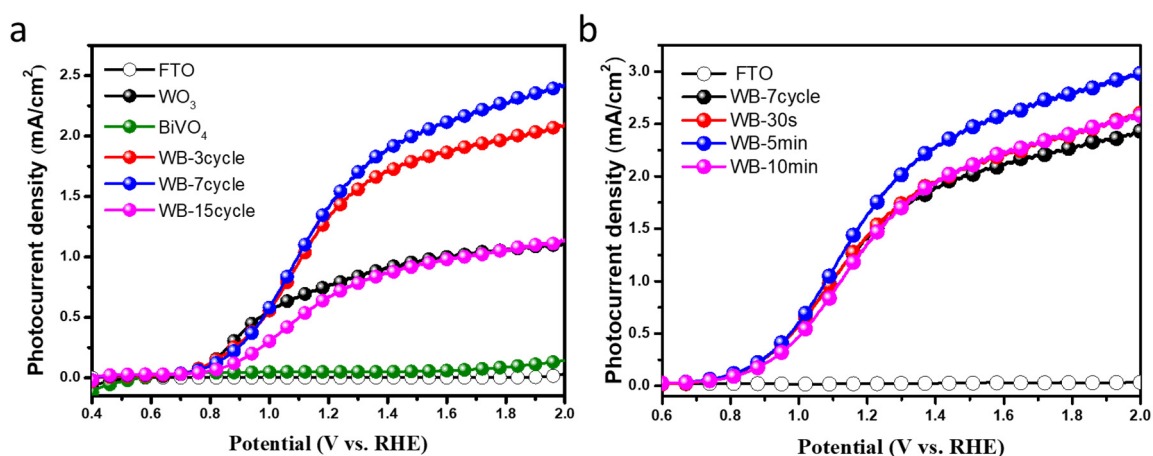


Figure 4. I-V curves for (a) FTO, WO_3 , BiVO_4 , WB-3cycle, WB-7cycle, and WB-15cycle samples and (b) FTO, WB-7cycle, WB-30s, WB-5min, and WB-10min samples.

2.3. Mechanism for the Enhanced PEC Performance

To monitor the local microstructure change of the FTO/ WO_3 / BiVO_4 samples after post-treatment by NaOH solution, TEM, and HR-TEM measurements were conducted with the results shown in Figure 5 and Figure S6. From the element mapping images in Figure S6, the BiVO_4 particles were successfully grown on the surface of WO_3 nanoflakes with relatively uniform distribution. HR-TEM measurements were focused on the surface of BiVO_4 particles (Figure 5a,b). The lattice fringe of 0.316 nm for WB-7cycle and 0.46 nm for WB-5min could be indexed to the (103) and (011) planes, respectively, further verifying the BiVO_4 crystal structure. More importantly, the BiVO_4 particles in WB-5min have much sharper edges compared to WB-7cycle, as outlined in the HR-TEM images. The polishing of the crystal boundary may activate the surface of BiVO_4 and lead to enhancement of solar conversion.

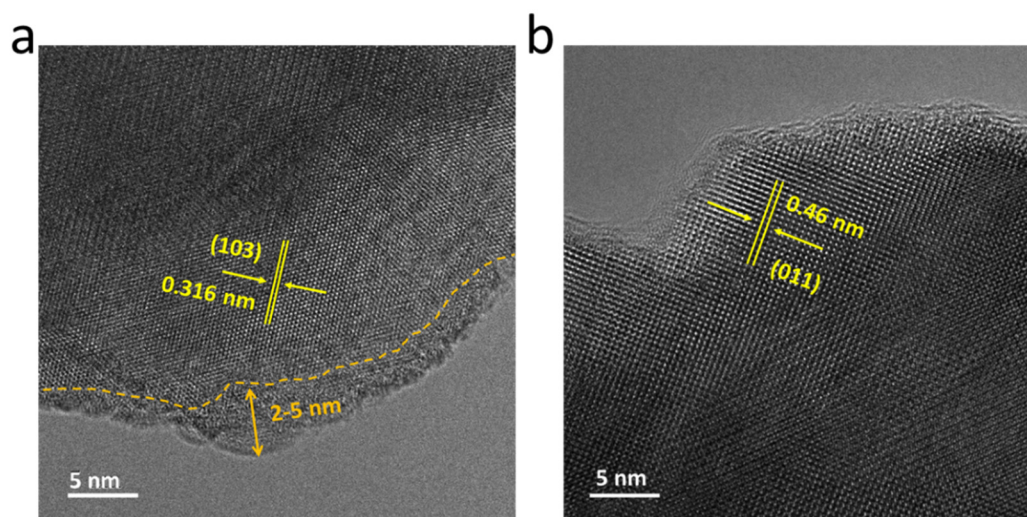


Figure 5. HR-TEM images of (a) WB-7cycle and (b) WB-5min samples.

X-ray photoelectron spectra (XPS) were collected for WB-7cycle and WB-5min to gain more insights into the surface chemical states (Figure 6). The peak of O 1s in WB-5min showed no obvious difference compared to that in the pure FTO/ WO_3 / BiVO_4 sample (Figure 6a), but the intensity of the

V 2p peak slightly increased (Figure 6b). In addition, the signal of Bi 4f exhibited a major increase after post-treatment (Figure 6c). As the post-treatment with NaOH solution could not cause redox reactions, the surface chemical states with no obvious change should be expected. With the XPS and HR-TEM results, it is reasonable to speculate that surface molecular arrangement of WB-5min should be reconstructed after surface burnishing of the amorphous layer, resulting in improved surface chemistry for photoconversion. To gain more information, the EIS was tested and shown in Figure 6d. The arc radius of WB-5min is smaller than those of WO₃ and WB-7cycle samples, illustrating the enhanced charge transport and accelerated surface reactions. The improved electrical properties of WB-5min should be ascribed to the surface burnishing of BiVO₄.

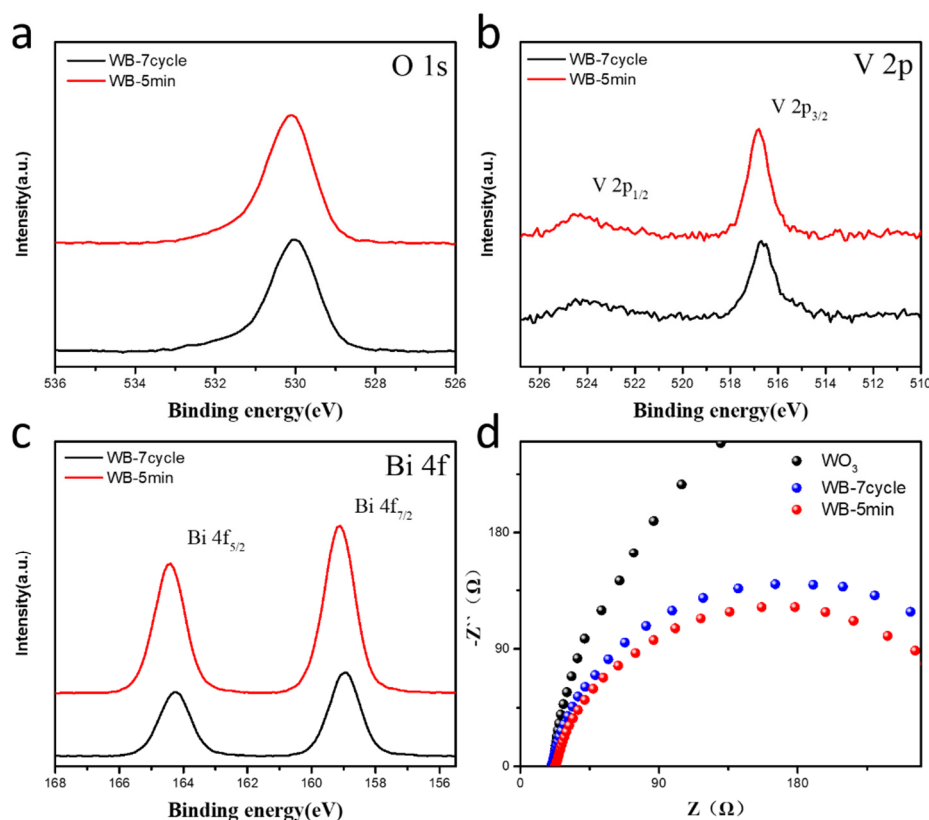


Figure 6. XPS spectra with (a) O 1s, (b) V 2p and (c) Bi 4f signals of WB-7cycle and WB-5min samples. (d) EIS plots of WO₃, WB-7cycle, and WB-5min samples.

3. Experimental Section

3.1. Materials

Sodium tungstate dehydrate (Na₂WO₄·2H₂O, 99.5%), hydrogen peroxide solution (H₂O₂, 30%), poly (vinyl alcohol) (PVA, 98%–99%), oxalic acid dihydrate (H₂C₂O₄·2H₂O, ≥99.5%), bismuth nitrate pentahydrate (BiN₃O₉·5H₂O, 99%), acetate (C₂H₄O₂, 99.7%), acetylacetonone (≥99.5%) were purchased from Aladdin Bio-Chem Technology Company, Shanghai, China. Vanadyl acetylacetonate (98%) was purchased from Sigma-Aldrich Sigma-Aldrich, St. Louis, MO, USA. Hydrochloric acid (HCl, 36%–38%) was purchased from Dong Jiang Reagent, Dongguan, China. All chemicals were used without further purification.

The FTO (2 cm × 1 cm) glass substrates were cleaned with ethanol and acetone mixture solution (1:1 by vol%) with sonication for 10 min. Then, the substrates were put into mixture solution of sulfuric acid and hydrogen peroxide (7:3 by vol%) for 10 min to make their surface hydrophilic.

3.2. Synthesis of WO₃ Seed Samples on FTO Substrates

First, 1.65 g Na₂WO₄·2H₂O was dissolved in 25 mL deionized (DI) water. After the addition of 3 mL HCl, precipitate was occurred with yellow color. Then the powder was washed through centrifugation at 5000 rpm 10 min for three times. The powder was re-dissolved in 5 mL H₂O₂ with 0.5 g PVA and 10 mL DI water. After ultra-sonication for 30 min, the solution was diluted to 30 mL with the addition of DI water. Then, 100 µL of the diluted solution was spin coated on top of FTO substrates with 3000 rpm for 1 min. Finally, the WO₃ seed samples could be obtained following thermal annealing at 500 °C in a muffle furnace for 2 h.

3.3. Synthesis of WO₃ Nanoflakes

0.1 g Na₂WO₄·2H₂O was dissolved in 45 mL DI water. After the addition of 4 mL HCl in the above solution, yellowish precipitate was obtained. Then 0.54 g H₂C₂O₄·2H₂O was added in the above solution under magnetic stirring until the precipitate was dissolved, with subsequent dilution to 135 mL. Next, 30 mL of the prepared precursor solution was transferred to a stainless steel autoclave. In addition, one piece of WO₃ seed sample was immersed in the solution and tilted on the container wall with the seed layer facing downward. The autoclave was sealed and kept at 180 °C for 8 h. After cooling to room temperature, the samples were rinsed with DI water. Finally, WO₃ nanoflakes could be obtained after annealing at 500 °C in a muffle furnace for 2 h.

3.4. Synthesis of FTO/WO₃/BiVO₄ Photoanodes

The precursor of BiVO₄ was prepared at first. 0.173 g BiN₃O₉·5H₂O and 0.095 g vanadyl acetate were dissolved in mixture solution consisted of 4.46 mL acetylacetone and 0.54 mL glacial acetic acid with sonication for 10 min. Then, FTO/WO₃/BiVO₄ photoanodes were prepared through spin-coating process. 25 µL precursor solution of BiVO₄ was coated on one piece of WO₃ sample with spin rate of 2000 rpm for 30 s and maintained at 400 °C for 2 min. The above process with one-time spin-coating was referred to as one cycle. Three kinds of FTO/WO₃/BiVO₄ photoanodes were prepared with different coating times of BiVO₄ precursor, as 3 cycles, 7 cycles, and 15 cycles. The above prepared samples were moved to muffle furnace and annealed at 450 °C for 2 h to obtain the final FTO/WO₃/BiVO₄ photoanodes. In addition, BiVO₄ film sample, as control group, was fabricated by dropping 25 µL BiVO₄ precursor directly on FTO substrate with further annealing at 450 °C for 2 h.

3.5. Post-Modification of FTO/WO₃/BiVO₄ Photoanodes

From the PEC performance, the 7 cycles FTO/WO₃/BiVO₄ sample performed the primarily highest photocurrent density. Thus, post-modification process will proceed by using 7 cycles FTO/WO₃/BiVO₄ samples, which were soaked in 0.2 M NaOH solution for 30 s, 5 min, 10 min, with 5 min as the best condition. The post-modified samples were known as WB-30s, WB-5min, and WB-10min. Then, the samples were rinsed with DI water and dried at room temperature.

3.6. Characterizations

The morphologies were characterized by Scanning Electron Microscope (SEM, ZEISS SUPRA[®] 55, Carl Zeiss, Jena, Germany) at an acceleration voltage of 5 KV. The crystal structure was determined by X-ray diffraction (XRD, D8 Advance, Bruker, Karlsruhe, Germany). The internal microstructure was analyzed by Transmission Electron Microscopy (TEM, JEM-3200FS, JEOL, Tokyo, Japan). X-ray photoelectron spectroscopy (XPS, ESCALAB 250Xi, Thermo Fisher, Waltham, MA, USA) was used to determine the surface chemical state and valence state. The entire XPS measurement was performed under ultra-vacuum condition, and the typical peak for C 1s of 284.8 eV was used for calibration. UV-Vis absorption spectrum was measured by UV-vis spectrophotometer (UV-2600, Shimadzu, Suzhou, China).

3.7. Photoelectrochemical Measurement

The PEC performance was measured using a typical three-electrode system with a transparent quartz glass as the reactor at room temperature. The samples, Pt foil and Ag/AgCl (saturated KCl) electrode were used as working electrode, counter electrode, and reference electrode, respectively. The photocurrent densities were measured in 0.5 M Na₂SO₄ (pH = 6.8) solution by using electrochemical workstation (CHI660e) under AM 1.5G simulated sunlight illumination. The light power of the solar simulator is calibrated using standard silicon cells. In addition, in order to improve the conductivity of all the samples, the top of the samples were coated with silver paste. The measuring area of the samples immersed in the liquid was kept at 1 cm² to accurately evaluate the photo- and dark-current value [38,39]. The measured potentials were converted to RHE potential with the following equation [40]:

$$E_{\text{RHE}} = E_{\text{Ag/AgCl}} + E^{\circ}_{\text{Ag/AgCl}} + 0.059 \text{ pH} \quad (1)$$

where E_{RHE} stands for calculated potential vs. RHE, $E_{\text{Ag/AgCl}}$ stands for the measured potential, and the value of $E^{\circ}_{\text{Ag/AgCl}}$ is 0.197 V at 25 °C.

The electrochemical impedance spectroscopy (EIS) was tested at 1.23 V vs. RHE with an Alternating Current (AC) voltage amplitude of 5 mV and frequency range of 0.1–10 kHz under simulated sunlight irradiation.

4. Conclusions

In summary, a FTO/WO₃/BiVO₄ heterojunction has been fabricated via hydrothermal and spin-coating methods and post-modification by NaOH solution. After adjusting the amount of BiVO₄ nanoparticles and post-modification time, FTO/WO₃/BiVO₄ heterojunction with 7 cycle spin-coating and 5min treatment produced the highest photocurrent of about 1.75 mA/cm² at 1.23 V vs. RHE, which is more than two times that for WO₃. The enhanced solar conversion performance should be caused by the facilitated charge transport and surface reaction kinetics, according to the surface burnishing of BiVO₄.

Supplementary Materials: The following are available online at <http://www.mdpi.com/2073-4344/10/5/556/s1>, Figure S1: SEM images of WO₃ nanoflakes. Figure S2: SEM images 7 layers WO₃/BiVO₄ with different treatment time by NaOH solution, as (a) 30 s, (b) 5 min and (c) 10 min. Figure S3: XRD pattern of pure BiVO₄ film. Figure S4: Band gap of WO₃, WB-7c, and WB-5min. Figure S5: Charge transfer diagram. Figure S6: (a) TEM image and (b–e) elements mapping of WB-7cycle sample.

Author Contributions: Conceptualization, Z.X. and M.M.; methodology, R.W.; software, Y.C. and B.W.; validation, Y.C. and W.T.; formal analysis, B.W. and R.W.; investigation, Y.C.; resources, J.L.; data curation, M.M.; writing—original draft preparation, Y.C.; writing—review and editing, Z.X. and M.M.; visualization, J.L.; supervision, M.M.; project administration, M.M.; funding acquisition, J.L. All authors have read and agreed to the published version of the manuscript.

Funding: This research was funded by National Natural Science Foundation of China (21905298, 31700835), Shenzhen Science and Technology Innovation Committee (JCYJ20190807164205542, JCYJ20190807164803603), and SIAT Innovation Program for Excellent Young Researchers (201807).

Conflicts of Interest: The authors declare no conflict of interest. The funders had no role in the design of the study; in the collection, analyses, or interpretation of data; in the writing of the manuscript, or in the decision to publish the results.

References

1. Fujishima, A.; Honda, K. Electrochemical Photolysis of Water at a Semiconductor Electrode. *Nature* **1972**, *238*, 37–38. [[CrossRef](#)] [[PubMed](#)]
2. Chen, X.; Shen, S.; Guo, L.; Mao, S.S. Semiconductor-based Photocatalytic Hydrogen Generation. *Chem. Rev.* **2010**, *110*, 6503–6570. [[CrossRef](#)] [[PubMed](#)]
3. Chen, X.; Zhang, Z.; Chi, L.; Nair, A.K.; Shangguan, W.; Jiang, Z. Recent Advances in Visible-Light-Driven Photoelectrochemical Water Splitting: Catalyst Nanostructures and Reaction Systems. *Nano Micro Lett.* **2016**, *8*, 1–12. [[CrossRef](#)] [[PubMed](#)]

4. Wang, R.; Bai, J.; Li, Y.; Zeng, Q.; Li, J.; Zhou, B. BiVO₄/TiO₂(N₂) Nanotubes Heterojunction Photoanode for Highly Efficient Photoelectrocatalytic Applications. *Nano Micro Lett.* **2016**, *9*, 13–21. [[CrossRef](#)]
5. Grätzel, M. Photoelectrochemical cells. *Nature* **2001**, *414*, 338–344. [[CrossRef](#)]
6. Shao, M.; Ning, F.; Wei, M.; Evans, D.G.; Duan, X. Hierarchical Nanowire Arrays Based on ZnO Core–Layered Double Hydroxide Shell for Largely Enhanced Photoelectrochemical Water Splitting. *Adv. Funct. Mater.* **2014**, *24*, 580–586. [[CrossRef](#)]
7. Kim, T.; Choi, K.-S. Nanoporous BiVO₄ Photoanodes with Dual-Layer Oxygen Evolution Catalysts for Solar Water Splitting. *Science* **2014**, *343*, 990–994. [[CrossRef](#)]
8. Wang, G.; Wang, H.; Ling, Y.; Tang, Y.; Yang, X.; Fitzmorris, R.C.; Wang, C.; Zhang, J.Z.; Li, Y. Hydrogen-Treated TiO₂ Nanowire Arrays for Photoelectrochemical Water Splitting. *Nano Lett.* **2011**, *11*, 3026–3033. [[CrossRef](#)]
9. Dias, P.; Lopes, T.; Meda, L.; Andrade, L.; Mendes, A. Photoelectrochemical water splitting using WO₃ photoanodes: The substrate and temperature roles. *Phys. Chem. Chem. Phys.* **2016**, *18*, 5232–5243. [[CrossRef](#)]
10. Yu, W.; Chen, J.; Shang, T.; Chen, L.; Gu, L.; Peng, T. Direct Z-scheme g-C₃N₄/WO₃ photocatalyst with atomically defined junction for H₂ production. *Appl. Catal. B Environ.* **2017**, *219*, 693–704. [[CrossRef](#)]
11. Su, J.; Guo, L.; Bao, N.; Grimes, C. Nanostructured WO₃/BiVO₄ Heterojunction Films for Efficient Photoelectrochemical Water Splitting. *Nano Lett.* **2011**, *11*, 1928–1933. [[CrossRef](#)] [[PubMed](#)]
12. Monforta, O.; Raptisb, D.; Satrapinsky, L.; Rochc, T.; Plescha, G.; Lianosb, P. Production of hydrogen by water splitting in a photoelectrochemical cell using a BiVO₄/TiO₂ layered photoanode. *Electrochim. Acta* **2017**, *251*, 244–249. [[CrossRef](#)]
13. González-Borrero, P.P.; Sato, F.; Medina, A.N.; Baesso, M.L.; Bento, A.C.; Baldissera, G.; Persson, C.; Niklasson, G.A.; Granqvist, C.G.; da Silva, A.F. Optical band-gap determination of nanostructured WO₃ film. *Appl. Phys. Lett.* **2010**, *96*, 061909. [[CrossRef](#)]
14. Hodes, G.; Cahen, D.; Manassen, J. Tungsten trioxide as a photoanode for a photoelectrochemical cell (PEC). *Nature* **1976**, *260*, 312–313. [[CrossRef](#)]
15. Dong, P.; Hou, G.; Xi, X.; Shao, R.; Dong, F. WO₃-based photocatalysts: Morphology control, activity enhancement and multifunctional applications. *Environ. Sci. Nano* **2017**, *4*, 539–557. [[CrossRef](#)]
16. Mi, Q.; Zhanaidarova, A.; Brunschwig, B.S.; Gray, H.B.; Lewis, N.S. A quantitative assessment of the competition between water and anion oxidation at WO₃ photoanodes in acidic aqueous electrolytes. *Energy Environ. Sci.* **2012**, *5*, 5694–5700. [[CrossRef](#)]
17. Fu, J.; Xu, Q.; Low, J.; Jiang, C.; Yu, J. Ultrathin 2D/2D WO₃/g-C₃N₄ step-scheme H₂-production photocatalyst. *Appl. Catal. B Environ.* **2019**, *243*, 556–565. [[CrossRef](#)]
18. Zhang, J.; Ma, H.; Liu, Z. Highly efficient photocatalyst based on all oxides WO₃/Cu₂O heterojunction for photoelectrochemical water splitting. *Appl. Catal. B Environ.* **2017**, *201*, 84–91. [[CrossRef](#)]
19. Wang, S.; Chen, P.; Yun, J.-H.; Hu, Y.; Wang, L. An Electrochemically Treated BiVO₄ Photoanode for Efficient Photoelectrochemical Water Splitting. *Angew. Chem. Int. Ed.* **2017**, *56*, 8500–8504. [[CrossRef](#)]
20. Rao, P.M.; Cai, L.; Liu, C.; Cho, I.S.; Lee, C.H.; Weisse, J.M.; Yang, P.; Zheng, X. Simultaneously Efficient Light Absorption and Charge Separation in WO₃/BiVO₄ Core/Shell Nanowire Photoanode for Photoelectrochemical Water Oxidation. *Nano Lett.* **2014**, *14*, 1099–1105. [[CrossRef](#)]
21. Xia, L.; Bai, J.; Li, J.; Zeng, Q.; Li, X.; Zhou, B. A highly efficient BiVO₄/WO₃/W heterojunction photoanode for visible-light responsive dual photoelectrode photocatalytic fuel cell. *Appl. Catal. B Environ.* **2016**, *183*, 224–230. [[CrossRef](#)]
22. Kim, C.W.; Son, Y.S.; Kang, M.J.; Kim, D.Y.; Kang, Y.S. (040)-Crystal Facet Engineering of BiVO₄ Plate Photoanodes for Solar Fuel Production. *Adv. Energy Mater.* **2016**, *6*, 1501754. [[CrossRef](#)]
23. Wang, S.; Chen, P.; Bai, Y.; Yun, J.-H.; Liu, G.; Wang, L. New BiVO₄ Dual Photoanodes with Enriched Oxygen Vacancies for Efficient Solar-Driven Water Splitting. *Adv. Mater.* **2018**, *30*, 1800486. [[CrossRef](#)] [[PubMed](#)]
24. Ye, K.-H.; Wang, Z.; Gu, J.; Xiao, S.; Yuan, Y.; Zhu, Y.; Zhang, Y.; Mai, W.; Yang, S. Carbon quantum dots as a visible light sensitizer to significantly increase the solar water splitting performance of bismuth vanadate photoanodes. *Energy Environ. Sci.* **2017**, *10*, 772–779. [[CrossRef](#)]
25. Zhang, K.; Shi, X.; Kim, J.K.; Lee, J.S.; Park, J.H. Inverse opal structured α-Fe₂O₃ on graphene thin films: Enhanced photo-assisted water splitting. *Nanoscale* **2013**, *5*, 1939–1944. [[CrossRef](#)]
26. Xu, S.; Fu, D.; Song, K.; Wang, L.; Yang, Z.; Yang, W.; Hou, H. One-dimensional WO₃/BiVO₄ heterojunction photonodes for efficient photoelectrochemical water splitting. *Chem. Eng. J.* **2018**, *349*, 368–375. [[CrossRef](#)]

27. Pihosh, Y.; Turkevych, I.; Mawatari, K.; Asai, T.; Hisatomi, T.; Uemura, J.; Tosa, M.; Shimamura, K.; Kubota, J.; Domen, K.; et al. Nanostructured WO₃/BiVO₄ photoanodes for efficient photoelectrochemical water splitting. *Small* **2014**, *10*, 3692–3699. [[CrossRef](#)]
28. Zhang, T.; Su, J.; Guo, L. Morphology engineering of WO₃/BiVO₄ heterojunctions for efficient photocatalytic water oxidation. *CrystEngComm* **2016**, *18*, 8961–8970. [[CrossRef](#)]
29. Zhou, Y.; Zhang, L.; Lin, L.; Wygant, B.R.; Liu, Y.; Zhu, Y.; Zheng, Y.; Mullins, C.B.; Zhao, Y.; Zhang, X.; et al. Highly efficient photoelectrochemical water splitting from hierarchical WO₃/BiVO₄ nanoporous sphere arrays. *Nano Lett.* **2017**, *17*, 8012–8017. [[CrossRef](#)]
30. Jin, B.; Jung, E.; Ma, M.; Kim, S.; Zhang, K.; Kim, J.I.; Son, Y.; Park, J.H. Solution-processed yolk-shell-shaped WO₃/BiVO₄ heterojunction photoelectrodes for efficient solar water splitting. *J. Mater. Chem. A* **2018**, *6*, 2585–2592. [[CrossRef](#)]
31. Zhang, J.; Zhang, P.; Wang, T.; Gong, J. Monoclinic WO₃ nanomultilayers with preferentially exposed (002) facets for photoelectrochemical water splitting. *Nano Energy* **2015**, *11*, 189–195. [[CrossRef](#)]
32. Xie, Y.P.; Liu, G.; Yin, L.; Cheng, H.-M. Crystal facet-dependent photocatalytic oxidation and reduction reactivity of monoclinic WO₃ for solar energy conversion. *J. Mater. Chem.* **2012**, *22*, 6746–6751. [[CrossRef](#)]
33. Liu, G.; Yu, J.C.; Lu, G.Q.; Cheng, H.-M. Crystal facet engineering of semiconductor photocatalysts: Motivations, advances and unique properties. *Chem. Commun.* **2011**, *47*, 6763–6783. [[CrossRef](#)] [[PubMed](#)]
34. Derikvandi, H.; Nezamzadeh-Ejhieh, A. Increased photocatalytic activity of NiO and ZnO in photodegradation of a model drug aqueous solution: Effect of coupling, supporting, particles size and calcination temperature. *J. Hazard. Mater.* **2017**, *321*, 629–638. [[CrossRef](#)] [[PubMed](#)]
35. Ghattavi, S.; Nezamzadeh-Ejhieh, A. A brief study on the boosted photocatalytic activity of AgI/WO₃/ZnO in the degradation of Methylene Blue under visible light irradiation. *Desalin. Water Treat.* **2019**, *166*, 92–104. [[CrossRef](#)]
36. Cooper, J.K.; Gul, S.; Toma, F.M.; Chen, L.; Glans, P.A.; Guo, J.H.; Ager, J.W.; Yano, J.; Sharp, I.D. Electronic Structure of Monoclinic BiVO₄. *Chem. Mater.* **2014**, *26*, 5365–5373. [[CrossRef](#)]
37. Chae, S.Y.; Lee, C.S.; Jung, H.; Joo, O.-S.; Min, B.K.; Kim, J.H.; Hwang, Y.J. Insight into Charge Separation in WO₃/BiVO₄ Heterojunction for Solar Water Splitting. *ACS Appl. Mater. Interfaces* **2017**, *9*, 19780–19790. [[CrossRef](#)]
38. Ma, M.; Kim, J.K.; Zhang, K.; Shi, X.; Kim, S.J.; Moon, J.H.; Park, J.H. Double-Deck Inverse Opal Photoanodes: Efficient Light Absorption and Charge Separation in Heterojunction. *Chem. Mat.* **2014**, *26*, 5592–5597. [[CrossRef](#)]
39. Iandolo, B.; Hellman, A. The Role of Surface States in the Oxygen Evolution Reaction on Hematite. *Angew. Chem. Int. Ed.* **2014**, *53*, 13404–13408. [[CrossRef](#)]
40. Wang, S.; Chen, H.; Gao, G.; Butburee, T.; Lyu, M.; Thaweesak, S.; Yun, J.-H.; Du, A.; Liu, G.; Wang, L. Synergistic crystal facet engineering and structural control of WO₃ films exhibiting unprecedented photoelectrochemical performance. *Nano Energy* **2016**, *24*, 94–102. [[CrossRef](#)]

